Ocean Color Measurements from Landsat-8 OLI using SeaDAS

Bryan A. Franz[1], Sean W. Bailey[1,2], Norman Kuring[1], and P. Jeremy Werdell[1]

[1]NASA Goddard Space Flight Center, Greenbelt, Maryland, USA
[2]Futuretech Corporation, Greenbelt, Maryland, USA

ABSTRACT

The Operational Land Imager (OLI) is a multi-spectral radiometer hosted on the recently launched Landsat-8 satellite. OLI includes a suite of relatively narrow spectral bands at 30-meter spatial resolution in the visible to shortwave infrared that make it a potential tool for ocean color radiometry: measurement of the reflected spectral radiance upwelling from beneath the ocean surface that carries information on the biogeochemical constituents of the upper ocean euphotic zone. To evaluate the potential of OLI to measure ocean color, processing support was implemented in SeaDAS, which is an open-source software package distributed by NASA for processing, analysis, and display of ocean remote sensing measurements from a variety of satellite-based multi-spectral radiometers. Here we describe the implementation of OLI processing capabilities within SeaDAS, including support for various methods of atmospheric correction to remove the effects of atmospheric scattering and absorption and retrieve the spectral remote-sensing reflectance (Rrs; sr^{-1}). The quality of the retrieved Rrs imagery will be assessed, as will the derived water column constituents such as the concentration of the phytoplankton pigment chlorophyll *a*.

INTRODUCTION

We define ocean color as the spectral distribution of reflected visible solar radiation upwelling from beneath the ocean surface. Variations in this water-leaving "remote sensing" reflectance distribution, Rrs(λ), the ratio of radiance emerging from beneath the ocean surface to the solar irradiance reaching the ocean surface, are governed by the optically-active biological and chemical constituents of the upper ocean through their absorption and scattering properties. A primary driver for variations in ocean color is the concentration of the phytoplankton pigment chlorophyll *a* (C*a*; mg m^{-3}), and bio-optical algorithms have been developed that relate measurements of Rrs(λ) to C*a* that provide a proxy for phytoplankton biomass. Marine phytoplankton account for roughly half the net primary productivity on Earth, so ocean color measurements are critical to our understanding of planetary health and the global carbon cycle. Other bio-optical and biogeochemical properties that can be inferred from Rrs(λ) include spectral absorption by colored dissolved organic matter, concentrations of total suspended sediments, measurements of water clarity such as marine diffuse attenuation coefficient and euphotic depth, and the presence of harmful algal blooms. Ocean color thus also provides a valuable tool for monitoring changes in the marine environment that can directly impact human health and commerce, especially in coastal areas where much of the human population resides.

Landsat-8 (Irons et al. 2011) was launched into a sun-synchronous polar orbit on 11 February 2013, carrying with it the Operational Land Imager (OLI, Table 1). Pre-launch simulations (Pahlevan & Schott 2013, Gerace et al. 2013) demonstrated that the sensor, while primarily designed for land applications, has the potential to provide useful measurements of aquatic environments and marine optical properties. A significant advantage of OLI over existing ocean color capable missions is the 30-m spatial resolution, which is at least an order of magnitude higher than NASA's global missions

such as the Moderate Resolution Imaging Spectroradiometer (MODIS, Esaias et al. 1998) currently operating from the Aqua spacecraft (MODISA) and the Sea-viewing Wide Field-of-view Sensor (SeaWiFS, McClain et al. 2004) that operated from 1997 to 2010. Increased spatial resolution is of particular benefit in studying heterogeneous coastal and inland waters, where the typical 1-km resolution of existing global sensors cannot resolve the fine spatial structure of the water constituents or separate water from land near coasts and in narrow rivers and bays. Thus, OLI on Landsat-8 has the potential to make a valuable contribution to ocean color science and environmental monitoring capabilities for aquatic ecosystems, especially in coastal environments.

Table 1: *Landsat-8 OLI Mission and Sensor Characteristics*

OLI Start Date	8 March 2013
Spatial Resolution	30 m
Swath Width	185 km
Eq. Crossing Time	10am +/- 15 min
Repeat Frequency	16 days
Native Digitization	12 bit
Data Availability	within 24 hours
Data Policy	free and open

The measurement of ocean color from spaceborne instruments is challenging because the water-leaving signal is only a small fraction of the total signal reflected by the earth into the sensor field of view. Approximately 90% of the visible radiation observed by earth-viewing satellite sensors is sunlight reflected by air molecules and aerosols in the atmosphere. The removal of this atmospheric signal to retrieve $Rrs(\lambda)$ is referred to as atmospheric correction. NASA's Ocean Biology Processing Group (OBPG) distributes a software package called SeaDAS that provides the research community with a standardized tool for the production, display, and analysis of ocean color products from a host of earth-viewing multi-spectral radiometers. SeaDAS contains within it the multi-sensor Level-1 to Level-2 generator (l2gen) that can read Level-1 observed TOA radiances from a variety of sensors, perform the atmospheric correction process, and retrieve $Rrs(\lambda)$ and various derived geophysical properties. The l2gen code can be adapted to work with any sensor that has a sufficient set of spectral bands covering the blue to green region of the visible spectrum (i.e., 400nm to 600nm), with at least two bands in the near-infrared (NIR) to shortwave IR (SWIR) to support the atmospheric correction.

Table 2: *Landsat-8 OLI Spectral Bands and Signal to Noise Ratios*

	Band 1	Band 2	Band 3	Band 4	Band 5	Band 6	Band 7
Nominal Center (nm)	443	482	561	655	865	1609	2201
Width (nm)	16.0	60.1	57.4	37.5	28.2	84.7	186.7
Ltyp (W / m^2 µm sr)	69.8	55.3	27.5	13.4	4.06	0.353	0.0467
SNR at Ltyp	344	478	279	144	67	30	14

OLI has a sufficient set of spectral bands for ocean color retrievals (Table 2). Precise atmospheric correction also requires that radiometric performance (signal relative to noise) and digital resolution of the observed radiometry is sufficiently high to detect the relatively small water-leaving radiance signal above the sensor noise.   In the sections that follow we assess the radiometric performance of the OLI instrument for ocean color applications, and detail the adaptation of l2gen in SeaDAS to support OLI

atmospheric correction. We also present results of an initial system-level vicarious calibration, where match-ups to in situ radiometry are used to refine the Rrs(λ) retrieval performance of the combined OLI instrument and atmospheric correction process. Finally, we show some results of ocean color retrieval over the coastal and inland waters of Chesapeake Bay and compare with coincident MODISA retrievals and in situ measurements.

DATA AND SENSOR CHARACTERISTICS

OLI data is freely available for direct download or bulk ordering from the website of the U.S. Geological Survey (USGS), which operates the Landsat-8 mission. The observed top-of-atmosphere (TOA) radiances (Level-1T) are provided in GeoTIFF format, with each spectral band in a separate file that has been mapped to a common Universal Transverse Mercator (UTM) projection. The full suite of spectral band files are packaged into a compressed tape archive (tar) file that also includes a Landsat Metadata (MTL) file in text form containing scene-specific time and location information.

OLI is a push-broom CCD system with 14 separate detector assemblies aligned across the orbit track to create the swath of approximately 170-km width or nearly 7000 pixels. The 14 detector assemblies alternate between slightly forward-pointing and slightly aft-pointing, and the spectral bands are aligned along track such that the amount of forward and aft pointing varies by band. The effect is that each spectral band views the same point on the earth at a slightly different time, and with a slightly different atmospheric path (characterized by sensor zenith and azimuth angles), and the path angles alternate fore and aft across the swath. Cross-track variations in geolocation and spectral band registration are effectively removed by mapping of the native observations to a common UTM projection in the Level-1T product, but the TOA radiances retain characteristics of their observational geometry that must be considered in ocean color retrieval.

Accurate atmospheric correction over the comparatively dark ocean requires precise knowledge of the solar and viewing path geometry. For the bands of interest to ocean color, the spectral variation in view zenith and azimuth angle is on the order of 0.2-deg and can be safely ignored, but mean variation in solar and sensor zenith and azimuth across the swath must be known, and the fore and aft variation between detector assemblies must be accounted for, or significant along-track banding artifacts will be evident in the Rrs(λ) retrievals. The Level-1T data product does not include this additional geometry information, but James Storey (USGS/SGT), geometric calibration/validation lead for Landsat-8, provided the authors with software to estimate solar and viewing geometry for each scene pixel from information contained in the scene MTL file. This software was used to produce solar and viewing geometry for each scene pixel of each band of the Level-1T product, and this information was then band-averaged and written to a scene-specific geometry file. This ancillary geometry file is required for the ocean color processing described herein.

Accurate atmospheric correction and Rrs(λ) retrieval also requires a sensor with sufficient signal to noise ratio (SNR) over ocean waters to detect and differentiate the small water-leaving signal. OLI is the most advanced radiometer ever flown on a Landsat platform, with SNRs roughly an order-of-magnitude higher then the predecessor ETM+ instrument of Landsat-7 (Barsi et al. 2011, Morfitt et al. 2014). The SNRs reported for OLI, however, are based on radiances typical of land observations. To assess OLI performance over oceans, the sensor noise model of Morfitt et al. (2014) was applied to typical radiances (Ltyp) interpolated from values reported in Hu et al. (2012a), which were themselves based on average radiances observed by MODISA over ocean targets at approximately 45-deg solar

zenith angle. Using these Ltyps, the derived OLI SNRs (Table 2) can be directly compared to those of SeaWiFS and MODISA as also reported by Hu et al. (2012a). In general, the OLI SNRs are lower than those of SeaWiFS or MODISA, but visible-band SNRs are within 50% of SeaWiFS (specified or observed) and OLI SWIR-band SNRs are equally similar to comparable MODISA SWIR bands. The biggest discrepancy is at 865nm, where the OLI SNR of 67 is substantially lower than the SeaWiFS specification (287), but still within a factor of 3 of the observed SeaWiFS SNR reported by Hu et al. It should also be recognized that OLI observations are at a much higher spatial resolution than SeaWiFS or MODIS, and spatial averaging over a few pixels could significantly increase the SNRs (see study in Gerace et al. 2013). Similar SNRs were measured by Pahlevan et al. (2014) through statistical analysis of uniform OLI scenes over oceans. Based on SNR equivalency with successful heritage ocean color sensors, the OLI radiometric performance appears sufficient for many ocean color applications.

PROCESSING APPROACH

Atmospheric Correction Algorithm

While l2gen supports a variety of atmospheric correction methods, many of which can be applied to OLI, the default approach described here follows the NASA standard processing in use for all global ocean color missions. Namely, the TOA radiance over water, Lt(λ), is modeled as the sum of atmospheric, surface, and subsurface contributions as:

(1) $Lt(\lambda) = Lr(\lambda) + La(\lambda) + t(\lambda)Lf(\lambda) + T(\lambda)Lg(\lambda) + t(\lambda)Lw(\lambda)$

where λ is a sensor spectral band wavelength, Lr(λ) is Rayleigh scattering from air molecules, La(λ) is scattering from aerosols and Rayleigh-aerosol interactions, t(λ) and T(λ) are diffuse and direct atmospheric transmittance from surface to sensor, Lf(λ) is contribution from whitecaps and foam on the surface that is diffusely transmitted to the TOA, Lg(λ) is specular reflection (glint) from the surface that is directly transmitted to the sensor field of view, and Lw(λ) is the water-leaving radiance that is diffusely transmitted to the TOA. All terms are dependent on the viewing and solar path geometries. Gaseous transmittance terms are not shown for clarity, but atmospheric transmittance losses due to ozone and NO_2 are also considered.

Table 3: *Landsat-8 OLI Band-averaged Atmospheric Coefficients*

	Band 1	Band 2	Band 3	Band 4	Band 5	Band 6	Band 7
F_0 (W / m^2 µm)	1896.52	2003.96	1820.79	1550.38	950.63	247.55	85.46
τ_r (Rayleigh)	2.352E-01	1.685E-01	9.020E-02	4.793E-02	1.551E-02	1.284E-03	3.697E-04
D_p (Depolarization)	2.910E-02	2.874E-02	2.825E-02	2.792E-02	2.755E-02	2.724E-02	2.718E-02

The TOA radiances collected by OLI are measured over the full spectral band-pass of each sensor band, and thus all terms on the right-hand side of Eq. 1 must be modeled or derived for the sensor-specific spectral response functions (SRFs). OLI spectral response functions were obtained from http://landsat.gsfc.nasa.gov/?p=5779. The Rayleigh scattering term, which is the dominant contribution over the visible spectral regime, is determined from pre-computed look-up tables of Rayleigh reflectance that were derived through vector radiative transfer simulations (Ahmad et al. 2010) spanning a wide range of realistic solar and viewing geometries. The OLI SRFs were used to

derive band-pass-integrated solar irradiances (F_0), Rayleigh optical thicknesses (τ_r) and depolarization factors (D_p, Table 3), where solar irradiance is taken from Thuillier et al. (2003) and hyperspectral Rayleigh optical thickness was computed using the model of Bodaine et al. (1999) and assuming standard pressure of 1013.25mb, temperature of 288.15K, and CO_2 concentration of 360ppm. The band-integrated optical thicknesses and depolarization factors were then used in the radiative transfer simulations to derive the OLI sensor-specific Rayleigh tables. The glint and whitecap contributions are modeled from knowledge of the environmental conditions (pressure, windspeed) and the sensor SRFs.

The primary unknowns in Eq. 1 are the water-leaving radiances that we wish to retrieve and the aerosol radiance, which is highly variable and must be inferred from the observations. The estimation of aerosol radiance follows the method of Gordon and Wang (1994), with updated aerosol models and selection approach described in Ahmad et al. (2010). This approach uses a pair of bands in the NIR or SWIR, where water is highly absorbing and thus water-leaving radiance is negligible or can be accurately estimated (e.g., Bailey et al. 2010), thus allowing aerosol radiance to be directly retrieved. The spectral slope in measured aerosol radiance between the two NIR-SWIR bands is used to select the aerosol type from a set of pre-computed aerosol models (Ahmad et al. 2010), where the aerosol models were derived from vector radiative transfer simulations specific to the OLI spectral band centers (Table 2). The retrieved aerosol model is then used to extrapolate measured aerosol radiance into the visible spectral regime.

In practice, any pair of bands can be used in the aerosol model selection process, with the only requirement being that the water-leaving radiance signal can be considered negligible or known. Using our initial SeaDAS implementation, Vanhellemont et al. (2014) explored several combinations of OLI bands 5, 6, and 7 in the NIR and SWIR with comparable results. For this analysis, we chose to use the combination of OLI bands 5 and 7 (865nm and 2201nm, respectively), with any non-negligible water-leaving radiance derived using the iterative bio-optical modeling approach of Bailey et al. (2010). This choice takes advantage of the longest SWIR wavelength, where water absorption is strongest, to help separate the radiometric contribution of in-water sediments from aerosol contributions, while using the higher SNR and spectral separation of the NIR channel to determine aerosol type.

With $La(\lambda)$ known at all spectral bands, the water-leaving radiance can be computed as in Eq. 2, and then normalized to derive the water-leaving reflectance as in Eqs. 3 & 4, where $Ed(\lambda)$ is down-welling solar irradiance just above the sea surface, $t_0(\lambda)$ is the atmospheric diffuse transmittance from Sun to surface, $F_0(\lambda)$ is the mean extraterrestrial solar irradiance averaged over the OLI SRF, $f_0(\lambda)$ is the Earth-Sun distance correction for the time of the observation, and θ_0 is the solar zenith angle. Finally, $B(\lambda)$ is a bi-directional reflectance correction to account for effects of inhomogeneity of the sub-surface light field and reflection and refraction through the air-sea and sea-air interface (Morel et al. 2002).

(2) $\quad t(\lambda)Lw(\lambda) = Lt(\lambda) \ - [(Lr(\lambda) + La(\lambda) + t(\lambda)Lf(\lambda) + T(\lambda)Lg(\lambda) + La(\lambda)]$

(3) $\quad Rrs(\lambda) = Lw(\lambda)/Ed(\lambda)/B(\lambda)$

(4) $\quad Ed(\lambda) = t_0(\lambda) \ f_0(\lambda) \ F_0(\lambda) \ \cos(\theta_0)$

To remove the effect of sensor-specific spectral response from $Rrs(\lambda)$, the full-band-pass water-leaving radiances are adjusted to that for square 11-nm band-passes (Wang et al. 2001) located at the

nominal band centers (Table 2) using the model of Werdell et al. (2007). These nominal-band water-leaving radiances are then converted to Rrs(λ) using nominal-center-band-averaged mean solar irradiances (Franz et al. 2003).

Bio-optical Algorithm

The retrieved Rrs(λ) at each visible sensor wavelength provide the basis for many derived geophysical product algorithms. The standard NASA algorithm for Ca is a 3-band empirical Rrs(λ) band ratio algorithm (OC3, O'Reilly et al. 2000) that transitions to an empirical band-difference algorithm (OCI, Hu et al. 2012b) in clear waters. For OLI, the empirical coefficients were tuned using the NASA bio-Optical Marine Algorithm Dataset (NOMAD, Werdell and Bailey 2005). The Ca algorithm uses the 443, 561, and 655-nm bands for the band difference and the 443, 482, and 561-nm bands for the band ratio.

Vicarious Calibration

Given the stringent accuracy requirements of satellite ocean color retrievals for both the instrument calibration and the atmospheric correction algorithm, an additional vicarious calibration was developed. This temporally-independent but wavelength-specific calibration minimizes residual bias and enhances spectral consistency of the sensor + algorithm system under idealized conditions (Franz et al. 2007). The primary vicarious calibration source for all NASA ocean color missions is the Marine Optical Buoy (MOBY), operated by NOAA near Lanai Hawaii (Clark et al. 1997). A time-series of all OLI scenes covering the Lanai region was collected and filtered to find cases of relatively clear, cloud-free atmospheric conditions and negligible Sun glint. The full screening and averaging process is detailed in Franz et al. (2007). Two scenes were found to pass all screening criteria (Fig. 1), and vicarious calibration gains were derived for each (Table 4). For this initial evaluation, the calibration of the atmospheric correction bands at 865 and 2201nm was not altered.

Table 4: *OLI Vicarious Calibration Gains*

	Band 1	Band 2	Band 3	Band 4	Band 5	Band 6	Band 7
09 Jan 2014	1.01932	1.04007	1.00720	1.01239	1.0	0.94364	1.0
10 Feb 2014	1.01771	1.04022	1.00734	1.01740	1.0	0.91266	1.0
avg. gain	1.0185	1.0401	1.0073	1.0149	1.0	0.9282	1.0

The change in color between the two images in Fig. 1, which were collected about one month apart, is due to the difference in solar geometry and a change in the aerosol conditions.   Notably, the vicarious calibration was highly consistent between the two scenes, which suggests that the atmospheric modeling compensated well for the changes observed between the two dates. The average vicarious gain in each band (Table 4) was implemented for all subsequent processing.

RESULTS AND DISCUSSION

The atmospheric correction approach discussed above and the vicarious calibration from Table 4 were applied to a series of OLI Level-1T scenes collected over the Chesapeake Bay region. Rrs(443) and Rrs(561) retrievals from a partial OLI scene on 5 September 2013, focusing on the mouth of the Bay from Cape Charles to Virginia Beach and the inlets of the James and York Rivers, show very good agreement with co-incident Rrs(443) and Rrs(547) retrievals from MODISA (Fig. 2). The MODISA

data were collected on the same day and processed with the same atmospheric correction approach, but using the sensor-specific spectral response functions and a sensor specific vicarious calibration. Also evident in this comparison is the enhanced information content that 30-m spatial resolution provides relative to the > 1-km resolution of MODIS.

The Rrs(λ) retrievals from OLI were applied to the empirical Ca algorithm and compared with the equivalent product from MODISA (Fig. 3). In general, OLI Ca retrievals for this day over the main stem of the lower Chesapeake Bay region are lower than those retrieved from MODISA. Assuming MODISA is correct, this would suggest that the Rrs(443) or Rrs(482) retrievals are too high relative to Rrs(561), i.e. the spectral dependence is biased toward the blue, which may be due to uncertainty in the vicarious calibration or error in the aerosol retrieval. Unfortunately, there is also considerable uncertainty in the MODISA instrument calibration in the latter period of the mission (Franz et al. 2014), so interpretation of this result as error in the OLI retrieval should be made with caution.

The spatial detail of the OLI ocean color retrievals is well illustrated in Fig. 4, where the red, green, and blue Rrs(λ) products at 655, 561, and 443-nm, respectively, have been combined into a quasi true-color image. This image, collected on 28 February 2014, shows striking detail of the presence of suspended sediments and other optically active biogeochemical constituents around coastal landforms and where rivers enter the Bay. Sediment plumes, for example, are clearly evident offshore of the Potomac and Rappahannock Rivers despite February 2014 being an average year with regards to streamflow (United States Geological Survey 2014) and free of any notable winter storms. The barrier islands between Hills Bay and Winter Harbor (between the Rappahannock and York Rivers) show significant suspended sediment loads, likely either from advective oceanward transport from the Rappahannock River or from wind-driven resuspension. Likewise, some of the shallowest areas of Chesapeake Bay, e.g., east of Smith and Tangier Islands, show substantial (re)suspended sediment loads. The high spatial resolution and relatively high SNR of OLI makes it possible to resolve the spatial structure of these estuarine features.

To further demonstrate the advantage that OLI spatial resolution provides over MODIS, Fig. 5 shows the same Rrs(λ) composite zoomed in to the mouth of the Potomac River, with MODISA scan-pixel boundaries for the same day overlaid. The OLI images show fine detail in ocean color that cannot be resolved by the larger MODIS pixels. OLI thus provides an unprecedented opportunity to directly observe this MODIS sub-pixel variability in suspended sediments and organic material, which can provide valuable insight into uncertainties in MODIS ocean color retrievals and improved understanding of differences observed in validation match-ups to localized in situ measurements.

Rrs(λ) composite images and Ca retrievals were generated for five scenes obtained over Chesapeake Bay between September 2013 and April 2014 (Fig. 6). The general similarity of the ocean color images suggests good temporal stability of the OLI calibration and good performance of the atmospheric correction algorithm over a wide range of solar geometries. These five scenes represent all available relatively cloud-free, glint-free scenes of Chesapeake Bay currently available from OLI, and thus Fig. 6 provides an indication of the frequency at which a mid-latitude location may be monitored with OLI, considering cloudy days and the 16-day repeat cycle of Landsat-8. In general, OLI observations between late spring and early fall over mid-latitude oceans are dominated by Sun glint (specular reflection) that substantially degrades ocean color retrieval quality.

For a more quantitative assessment of OLI ocean color retrieval performance, the distribution of C*a* and Rrs(λ) retrievals over Chesapeake Bay was compared to same-day retrievals from MODISA. Following Werdell et al. (2009), data from the five scenes of Fig. 6 were geographically stratified into lower and middle Bay regions to produce the regional frequency distributions of Fig. 7. Also shown is the mean distribution from SeaWiFS over the mission lifespan (1997-2010), to provide additional context on expected range of values. Results show relatively good agreement between OLI and MODISA Rrs(λ) distributions, especially in the green (i.e., Rrs(561) of OLI compared with Rrs(547) of MODISA), and both sensors are in good agreement with the SeaWiFS mission mean. Agreement is not quite as good for the bluest band, with OLI Rrs(443) being elevated relative to MODISA Rrs(443). This gives rise to a larger blue/green ratio from OLI and thus lower C*a* retrievals relative to MODISA, as previously presented in Fig. 3. These differences may simply be the result of uncertainty in the OLI vicarious calibration derived from just two MOBY measurements, or the as yet uncorrected atmospheric correction bands, but again the discrepancy may be due to error in MODISA retrievals or simply differences in sampling. The C*a* values from OLI and MODISA in the middle Bay do straddle the range of values measured over previous years by SeaWiFS, and in fact the OLI retrievals of C*a* in the lower Bay are in very good agreement with expectation based on historical SeaWiFS retrievals. Also shown on Fig. 7 is the distribution of in situ C*a* measurements collected at regular spatial and temporal sampling intervals over a 26-year period from 1984 to 2010 (Chesapeake Bay Program 1993), showing that these OLI C*a* retrievals fall within the range of values expected from field observations.

CONCLUSIONS

OLI has the requisite spectral bands and sufficient radiometric performance to support ocean color applications. Atmospheric correction and ocean color product retrieval support for OLI has been incorporated into NASA's freely-distributed SeaDAS software package, and an initial system vicarious calibration has been performed. Evaluation of OLI ocean color retrieval over a time-series of Chesapeake Bay scenes demonstrated relatively good agreement with other ocean color sensors and with historical field measurements in the region. The observed agreement may further improve as instrument temporal calibration is refined and additional MOBY measurements are incorporated to reduce uncertainty in the OLI vicarious calibration, but these initial results clearly demonstrate that OLI can be a valuable tool for ocean color science and environmental monitoring applications, as well as for understanding the inherent uncertainty in lower-resolution ocean color sensors due to unresolved sub-pixel variability.
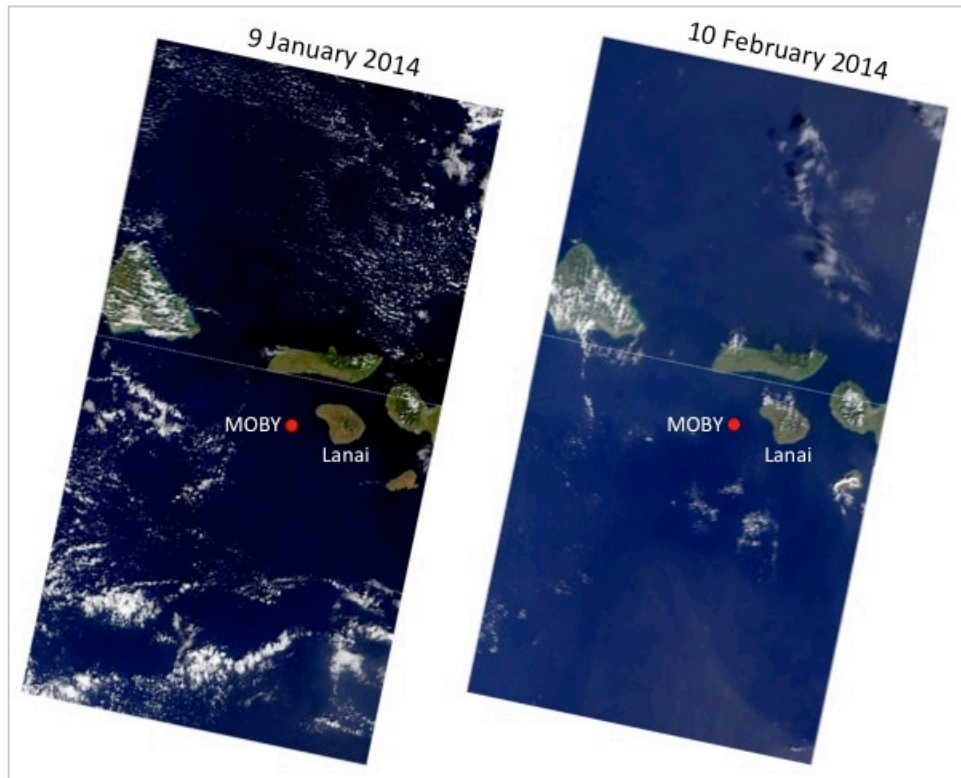
ACKNOWLEDGEMENTS

Figure 1: *OLI images over Lanai, Hawaii on 9 January and 10 February 2014 showing location of the NOAA Marine Optical Buoy (MOBY). Co-located data from MOBY and OLI on these dates were used in the OLI vicarious calibration.*
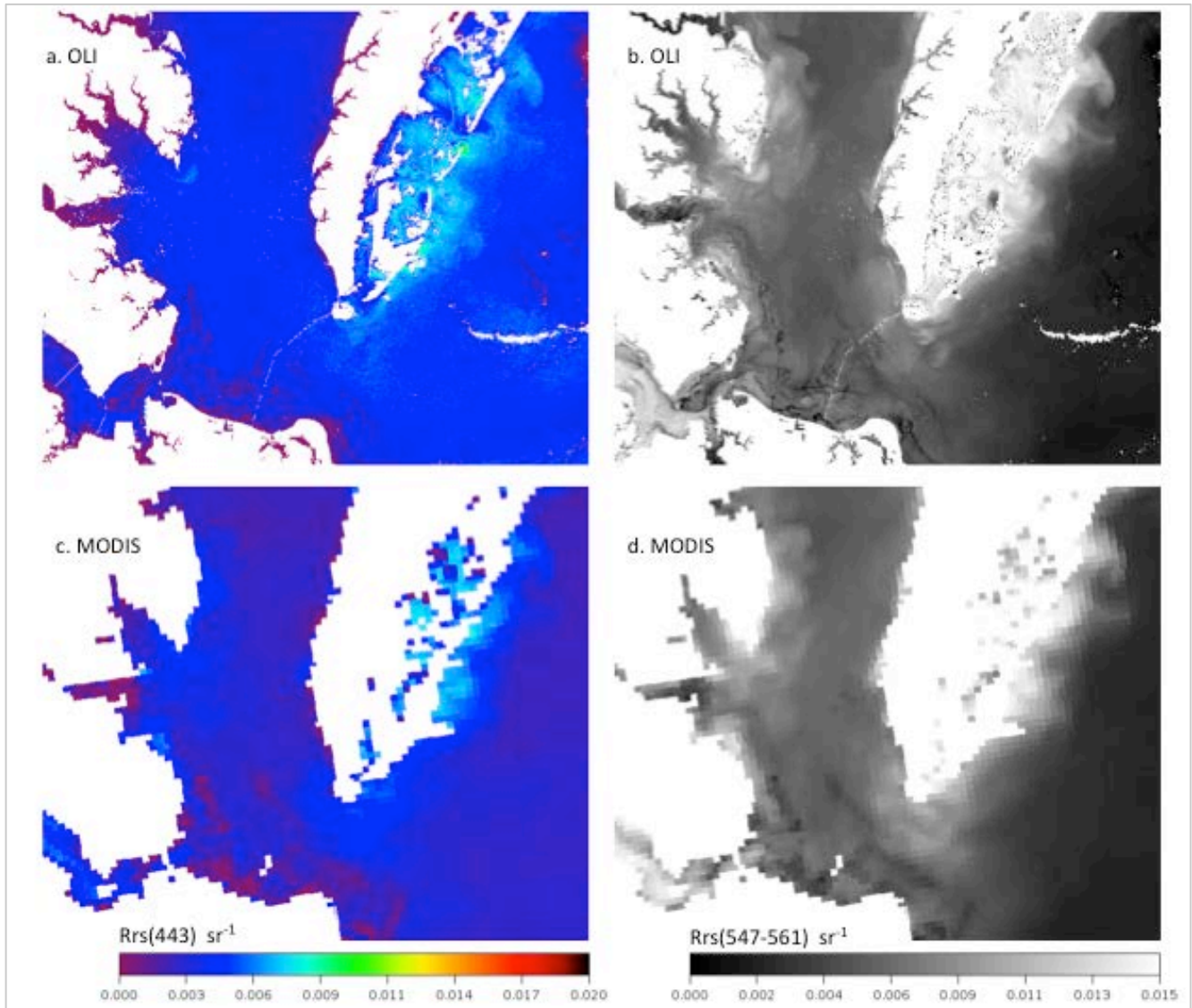
B.A. Franz, S.W. Bailey, N. Kuring, and P.J. Werdell, "Ocean Color Measurements from Landsat-8 OLI using SeaDAS," *Proc. Ocean Optics 2014*, Portland Maine (USA), 26-31 October 2014.

Figure 2: *Images of water-leaving reflectances, Rrs(443) and Rrs(561), retrieved from OLI over Chesapeake Bay on 5 September 2013, with MODIS Aqua retrievals of Rrs(443) and Rrs(547) shown for comparison. The MODIS data was collected on the same day, about 3 hours later. The Rrs(λ) was retrieved using standard NASA ocean color processing in SeaDAS.*

B.A. Franz, S.W. Bailey, N. Kuring, and P.J. Werdell, "Ocean Color Measurements from Landsat-8 OLI using SeaDAS," *Proc. Ocean Optics 2014*, Portland Maine (USA), 26-31 October 2014.
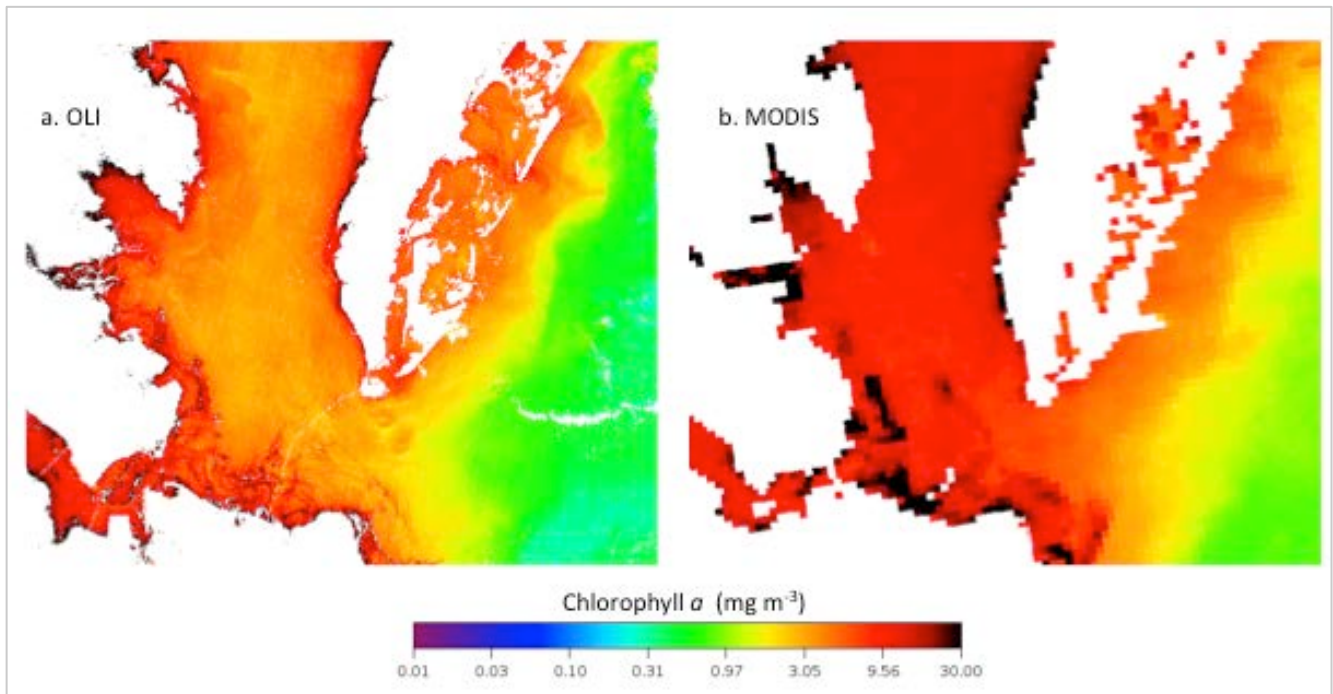
Figure 3: *Images of chlorophyll a concentration retrieved from OLI and MODIS Aqua over Chesapeake Bay on 5 September 2013. The MODIS data was collected on the same day, about 3 hours later. The chlorophyll a concentration was retrieved using standard NASA ocean color processing in SeaDAS.*
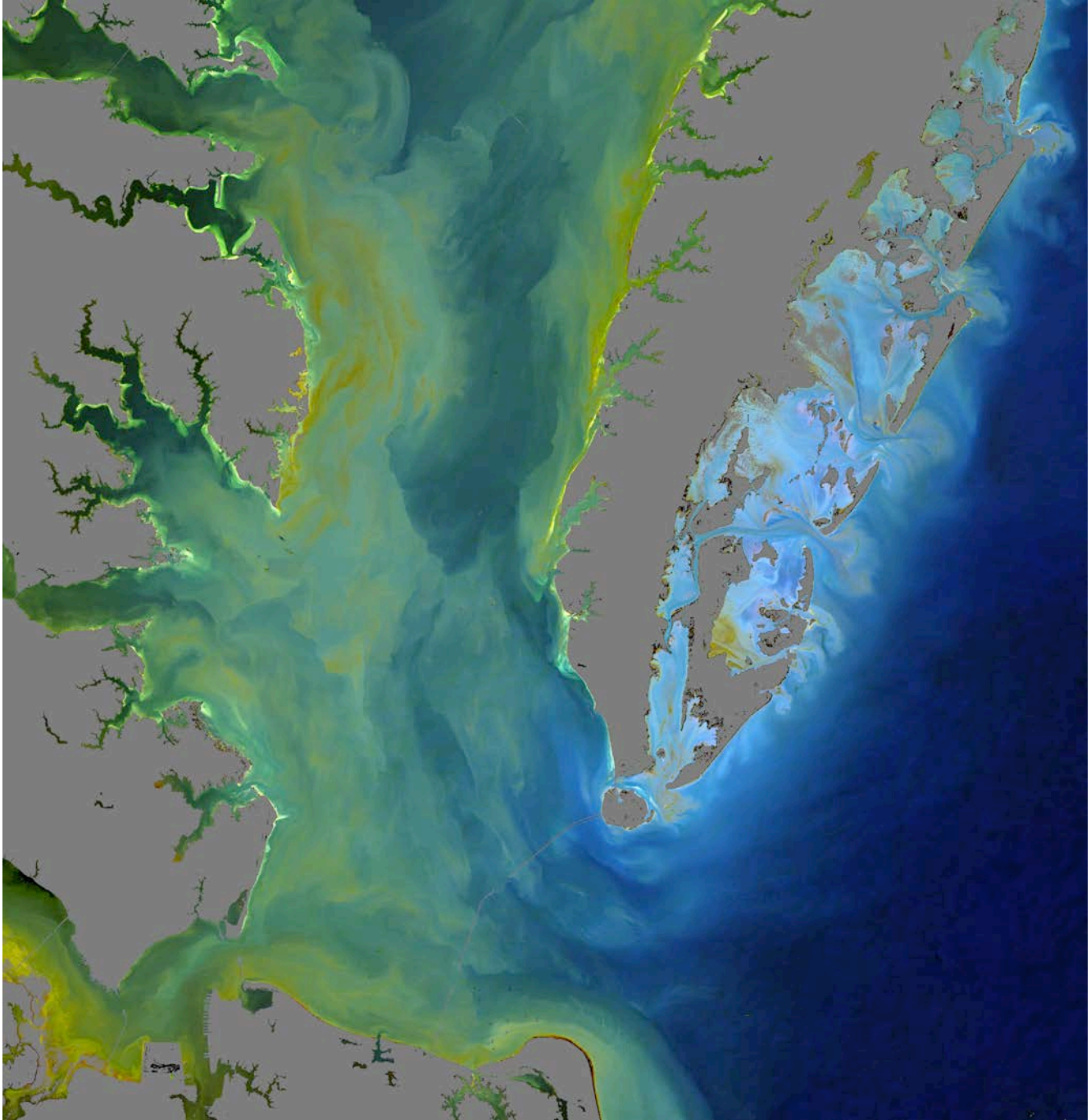
Figure 4: *Three-band water-leaving reflectance, Rrs(λ), composite image over the mouth of Chesapeake Bay showing detailed distribution patterns of sediments and colored organic matter that can be retrieved from OLI using standard NASA ocean color processing in SeaDAS. The composite was generated using the red, green, and blue reflectances at 655, 561, and 443nm, respectively.*
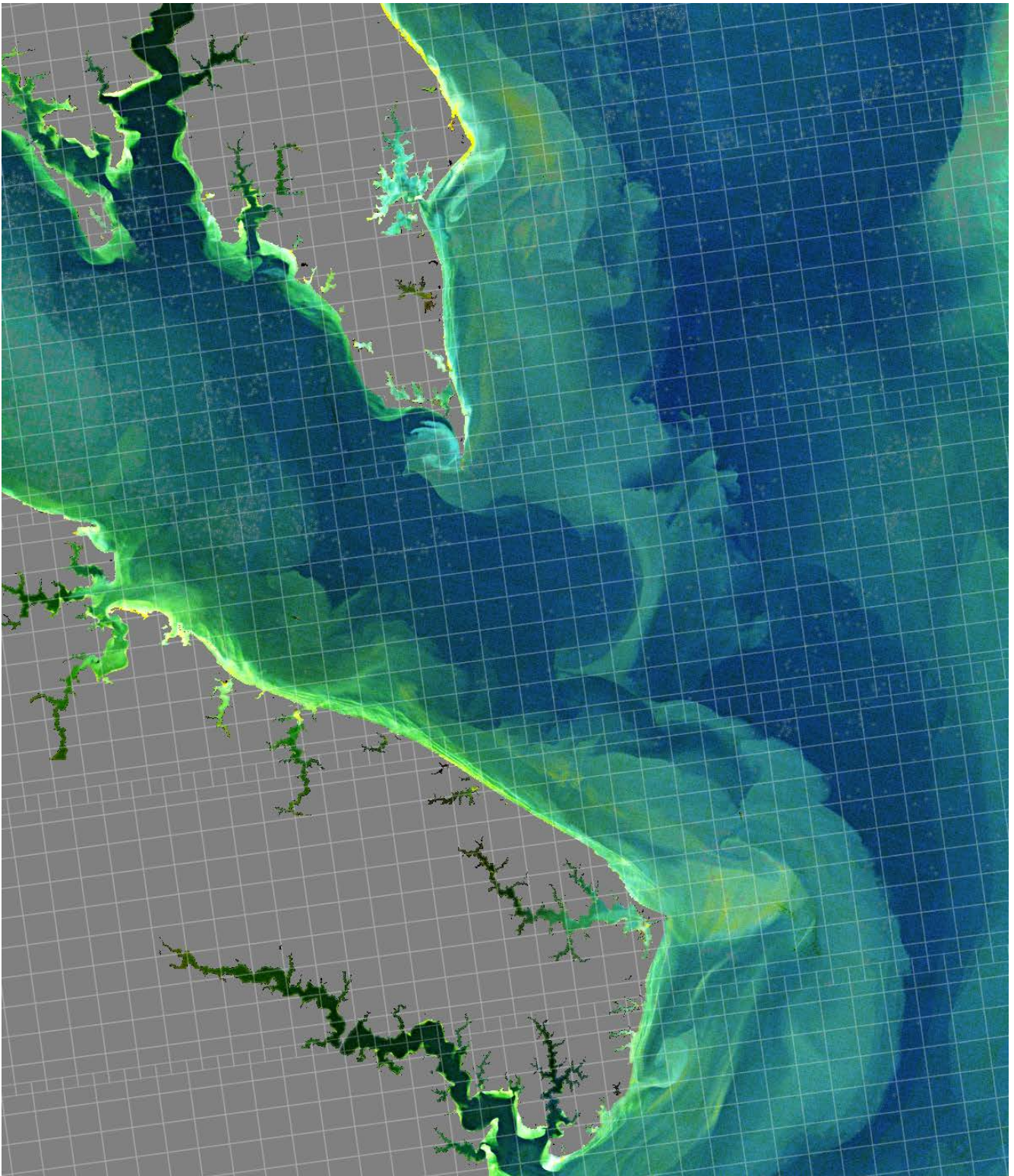
B.A. Franz, S.W. Bailey, N. Kuring, and P.J. Werdell, "Ocean Color Measurements from Landsat-8 OLI using SeaDAS," *Proc. Ocean Optics 2014*, Portland Maine (USA), 26-31 October 2014.

Figure 5: *Three-band water-leaving reflectance composite image from OLI at the location where the Potomac River enters Chesapeake Bay. MODIS Aqua scan pixel boundaries for the same date are overlaid to demonstrate the sub-pixel variability revealed by the higher spatial resolution of OLI. The Rrs(λ)were retrieved using standard NASA ocean color processing in SeaDAS, and red, green, and blue reflectances at λ=(655, 561, 443nm) were combined to form the image.*
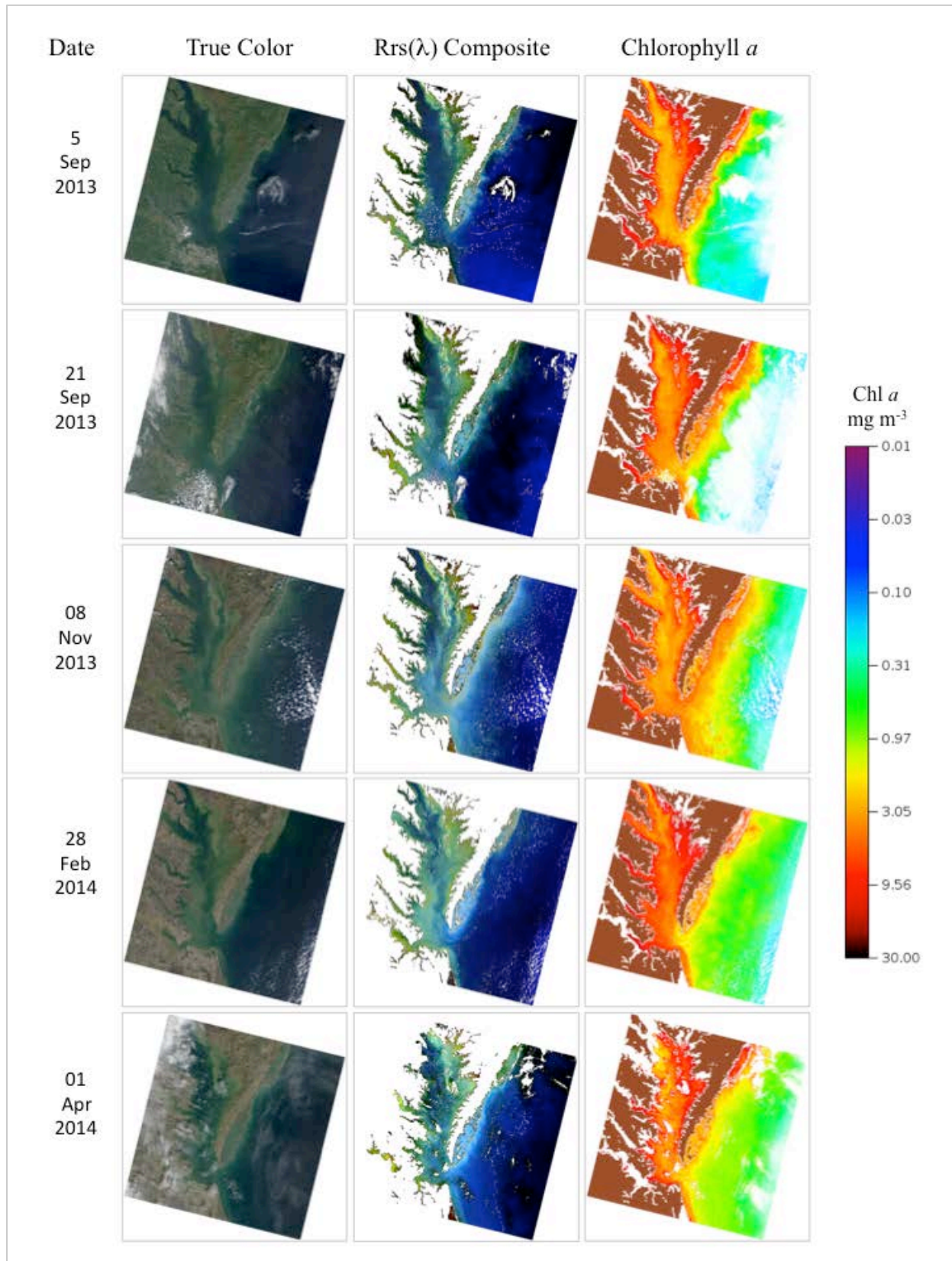
B.A. Franz, S.W. Bailey, N. Kuring, and P.J. Werdell, "Ocean Color Measurements from Landsat-8 OLI using SeaDAS," *Proc. Ocean Optics 2014*, Portland Maine (USA), 26-31 October 2014.

Figure 6: *OLI true-color images, Rrs(λ) composite images, and chlorophyll a retrievals from all available clear scenes over Chesapeake Bay.*
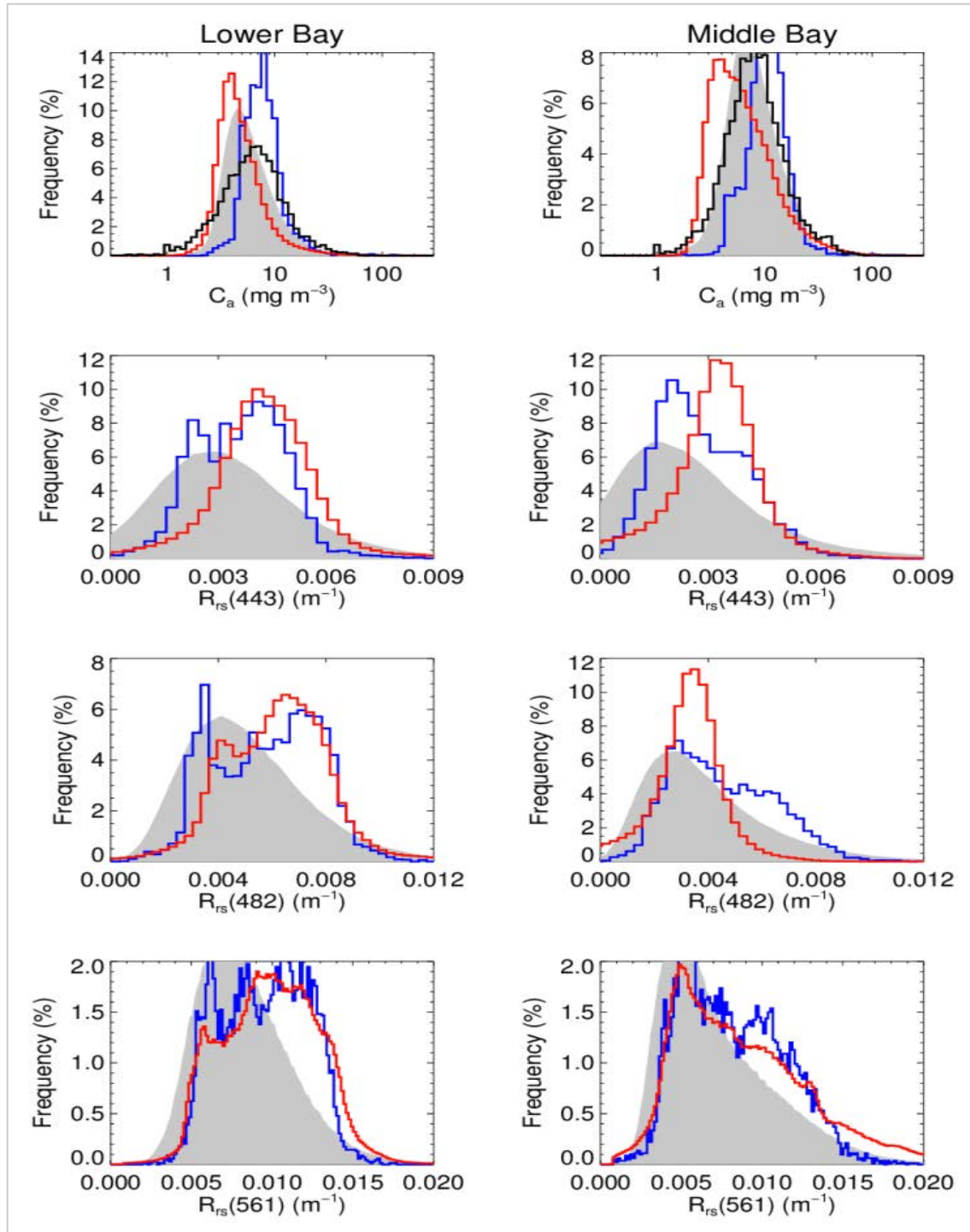
B.A. Franz, S.W. Bailey, N. Kuring, and P.J. Werdell, "Ocean Color Measurements from Landsat-8 OLI using SeaDAS," *Proc. Ocean Optics 2014*, Portland Maine (USA), 26-31 October 2014.

Figure 7: *Comparison of OLI, MODIS-Aqua, and SeaWiFS chlorophyll a and Rrs(λ) retrieval distributions in the middle and lower Chesapeake Bay, following Werdell et al. 2009. OLI (red) and MODIS (blue) data were collected over the same five dates shown in Fig. 6. SeaWiFS data (gray shaded) show the average over the mission lifetime (1997-2010). In situ chlorophyll a measurements shown in black were collected within the same region at regular spatial and temporal sampling intervals over the period 1984-2010 (Chesapeake Bay Program 1993).*

REFERENCES

Ahmad, Z., B.A. Franz, C.R. McClain, E.J. Kwiatkowska, J. Werdell, E.P. Shettle, and B.N. Holben (2010). New aerosol models for the retrieval of aerosol optical thickness and normalized water-leaving radiances from the SeaWiFS and MODIS sensors over coastal regions and Open Oceans, Appl. Opt., 49(29).

Bailey, S.W., B.A. Franz and P.J. Werdell (2010). Estimation of near-infrared water-leaving reflectance for satellite ocean color data processing. *Optics Express, 18,* 7521-7527.

Barsi, J.A., B.L. Markham, J.A. Pedelty (2011). The operational land imager: spectral response and spectral uniformity, SPIE Optical Engineering Applications, 81530G–81530G.

Bodhaine, B.A., N.B. Wood, E.G. Dutton, J.R. Slusser (1999). On Rayleigh Optical Depth Calculations. J. Atmos. Oceanic Technol., 16, 1854–1861.

Chesapeake Bay Program (1993). Guide to using Chesapeake Bay program water quality monitoring data. CBP/TRS 78/92 (pp. 127). Annapolis: Chesapeake Bay Program.

Clark, D. K., H. R. Gordon, K. J. Voss, Y. Ge, W. W. Broenkow, and C. Trees (1997). Validation of atmospheric correction over the oceans, J. Geo. Res. 102, 17209– 17217.

Esaias, W. E., M. R. Abbot, I. J. Barton, O. B. Brown, J. W. Campbell, K. L. Carder, D. K. Clark, R. H. Evans, F. E. Hoge, H. R. Gordon, W. M. Balch, R. Letelier, and P. J. Minnett (1998). An overview of MODIS capabilities for ocean science observations, IEEE Transactions on Geoscience and Remote Sensing 36, 1250–1265.

Franz, B.A., R.E. Eplee, Jr., S.W. Bailey, and M. Wang (2003). Changes to the atmospheric correction algorithm and retrieval of oceanic optical properties. NASA/TM-2003-206892, Vol. 22, NASA Goddard Space Flight Center, Greenbelt, Maryland, 29-33.

Franz, B.A., S.W. Bailey, P.J. Werdell, and C.R. McClain, F.S. (2007). Sensor-independent approach to vicarious calibration of satellite ocean color radiometry, Appl. Opt., 46 (22).

Franz, B.A., D.A. Siegel, M.J. Behrenfeld, P.J. Werdell (2014). Global ocean phytoplankton [in State of the Climate in 2013]. Bulletin of the American Meteorological Society, 95(7), S78-S80.

Gerace. A.D., J.R. Schott, R. Nevins (2013). Increased potential to monitor water quality in the near-shore environment with landsat's next-generation satellite. J. Appl. Remote Sens. 0001;7(1):073558-073558. doi:10.1117/1.JRS.7.073558.

Gordon, H.R., and Wang, M. (1994). Retrieval of water-leaving radiance and aerosol optical-thickness over the oceans with SeaWiFS – a preliminary algorithm. *Applied Optics*, 33, 443-452.

Hu, C., L. Feng, Z. Lee , C.O. Davis, A. Mannino, C.R. McClain, B.A. Franz (2012a). Dynamic range and sensitivity requirements of satellite ocean color sensors: learning from the past, Appl. Opt., Vol. 51, No. 25. doi:10.1364/AO.51.006045.

Hu, C., Z. Lee, and B.A. Franz (2012b). Chlorophyll-a algorithms for oligotrophic oceans: A novel approach based on three-band reflectance difference, J. Geophys. Res., 117, C01011.

Irons, J.R., J.L. Dwyer, J.A. Barsi (2012). The next Landsat satellite: The Landsat Data Continuity Mission, Remote Sens. Environ, 122, 11–21.

McClain, C.R., S. Hooker, and G.C. Feldman (2004). An overview of the SeaWiFS project and strategies for producing a climate research quality global ocean bio-optical time series *Deep-Sea Res. II*, *51*, 5-42.

Morfitt, R., B.L. Markham, E. Micijevic, P. Scaramuzza, J.A. Barsi, R. Levy, L. Ong, K. Vanderwerff (2014). OLI Radiometric Performance On-Orbit. Remote Sensing 2014, in press.

O'Reilly, J.E. and 24 co-authors (2000). SeaWiFS Postlaunch Calibration and Validation Analyses, Part 3, NASA Tech. Memo. 206892, Vol. 11, NASA Goddard Space Flight Center, Greenbelt, Maryland, pp 24.

Pahlevan, N., and J. Schott (2013). Leveraging EO-1 to Demonstrate Capability of New Generation of Landsat Sensors in Coastal/Inland Water Studies, IEEE J. of Selected Topics in Applied Earth Observations and Remote Sensing, 6 (2)**,** 360-374.

Pahlevan, N., Z-P. Lee, J. Wei, C.B. Schaaf, J.R. Schott, and A. Berk (2014). On-Orbit Radiometric Characterization of OLI (Landsat-8) for Application to Aquatic Remote Sensing, Remote Sensing of Environment, 154, 272-284. doi: 10.1016/j.rse.2014.08.001

Thuillier, G., M. Hersé, P. C. Simon, D. Labs, H. Mandel, D. Gillotay, and T. Foujols (2003). The solar spectral irradiance from 200 to 2400 nm as measured by the SOLSPEC spectrometer from the ATLAS 1-2-3 and EURECA missions, Solar Physics, 214(1): 1-22.

United States Geological Survey (2014), Estimated streamflow entering Chesapeake Bay, http://md.water.usgs.gov/waterdata/chesinflow/.

Vanhellemont, Q., S. Bailey, B.A. Franz, D. Shea (2014). Atmospheric Correction of Landsat-8 Imagery using SeaDAS, in proc. Sentinel-2 for Science, Frascati, Italy, 21-23 May 2014.

Wang, M., Franz, B.A., Barnes, R.A., and McClain, C.R. (2001). Effects of spectral bandpass on SeaWiFS-retrieved near-surface optical properties of the ocean. *Applied Optics*, 40: 343-348.

Werdell, P.J. and Bailey, S.W. (2005). An improved in situ bio-optical data set for ocean color algorithm development and satellite data product validation, Rem. Sens. Env., 98, 122-140.

Werdell, P.J., S.W. Bailey, B.A. Franz, A. Morel, and C.R. McClain (2007). On-orbit vicarious calibration of ocean color sensors using an ocean surface reflectance model, Appl. Opt. 46, 5649-5666.

Werdell, P.J., S.W. Bailey, B.A. Franz, L,W. Harding Jr., G.C. Feldman, C.R. McClain (2009). Regional and seasonal variability of chlorophyll-a in Chesapeake Bay as observed by SeaWiFS and MODIS-Aqua, Rem. Sens. Env., 113(6), 1319-1330.